



## Research paper

## Experiments and finite element analysis on a hybrid polymer gear rack

James D.S. Hooton<sup>a</sup>, David E.P. Gonçalves<sup>b</sup>, Carlos M.C.G. Fernandes<sup>a,b,\*</sup><sup>a</sup> Faculdade de Engenharia, Universidade do Porto, Rua Dr. Roberto Frias s/n, Porto, 4200-465, Portugal<sup>b</sup> INEGI, Campus da FEUP, Rua Dr. Roberto Frias 400, Porto, 4200-465, Portugal

## ARTICLE INFO

## Keywords:

Hybrid polymer gear  
Thermal expansion  
Finite element analysis  
Digital image correlation  
Interference fit  
Thermal contact conductance

## ABSTRACT

This article presents the results of experiments and finite element analysis on a hybrid polymer gear concept. The study aimed to investigate the effectiveness of the hybrid gear concept by using a rack tooth geometry.

The results of the experiments have shown that the hybrid gear concept improves the heat evacuation from the flank and root regions, potentially increasing the load-carrying capacity. Additionally, the results of the experiments were compared with those obtained from the finite element analysis to validate the numerical model. The results showed that the hybrid polymer gear rack exhibited good thermal performance, and the finite element analysis accurately predicted the behaviour of the gear rack specimens. The study also analyses the influence of the interference fit on the contact pressure and thermal contact conductance in a hybrid polymer gear concept, taking into account surface roughness and temperature. It provides insights for optimizing the press fit to ensure efficient heat dissipation in practical applications.

Overall, the study provides valuable insights into the potential use of hybrid polymer-metal materials in gear applications and supports the validity of the hybrid gear concept.

## 1. Introduction

In recent years, the use of polymer gears has grown quickly due to their economic potential and technical advantages over metallic gears in several applications. Polymer gears have a low production cost and can operate without grease or oil lubrication, which makes them perfect for non-lubricated applications, such as medical or laboratory devices, the food industry and household appliances. Additionally, due to their low density, polymer gears are lighter than steel, and thus can significantly reduce energy consumption and noise level in gearboxes [1,2]. An extensive review on the materials and the performance characteristics of polymer gears can be found in [3].

A major limitation common to several polymer materials is their low thermal conductivity and the strong dependence of their mechanical properties on the operating temperature. For these reasons, polymer gears are typically used in low-load transmission applications where the temperature of the teeth flanks is moderate [4]. The most common materials for gears are polyamides (PA) and polyacetal (POM). Some high-performance, heat resistant and high-temperature stable materials options are polyether ether ketone (PEEK), and polyimides (PI) [5,6].

According to Mao [7], the gear wear rate is much smaller if the gear operating temperature does not reach the material melting point. Kalin [8] also observed the important effect of the temperature on the fatigue life of POM gears. At high temperatures, polymers can undergo chemical degradation, causing a reduction in strength and stiffness. This degradation can also lead to a

\* Corresponding author at: Faculdade de Engenharia, Universidade do Porto, Rua Dr. Roberto Frias s/n, Porto, 4200-465, Portugal.

E-mail address: [cfernandes@fe.up.pt](mailto:cfernandes@fe.up.pt) (C.M.C.G. Fernandes).

change in the polymer's morphology, resulting in an increase in the coefficient of friction and wear rate. Therefore, it is crucial to consider the operating temperature range and select suitable materials for polymer gear applications to ensure reliable and durable performance [9]. The manufacturing quality of polymer gears also plays a crucial role in their performance and durability. Therefore, it is essential to ensure consistent manufacturing quality and proper quality control measures to minimize defects and ensure the desired gear performance [10,11].

The calculation of the load-carrying capacity of a polymer gear can be formulated as an optimization problem [12] that requires a precise quantification of its operating temperature. There are several analytical methods typically used to determine the bulk temperature of polymer gears [13–18]. While the analytical methods are easy and fast to implement they still present some noticeable limitations [19]. To overcome the limitations of the analytical methods, several numerical models have been proposed in literature [4,20–25]. The numerical models that rely on the finite element method (FEM) usually require state-of-the-art convective heat transfer coefficients to accurately predict the operating temperature. Roda-Casanova has proposed a set of coefficients to accurately determine the Nusselt number for different regions of a polymer gear based on computational fluid dynamics analysis [26].

To improve the thermal and mechanical properties of polymer gears under operation, new design techniques have been developed to enhance their performance. These techniques include modification to gear tooth geometry to minimize meshing power loss, adding cooling holes, combining different materials for the gear pair, or a hybrid gear design. Some of these ideas have been shown to increase the gear life cycle, reduce wear, increase durability and improve the thermal behaviour [1,27–29]. To replace conventional steel gears, hybrid metal-composite gears have been proposed to reduce mass and improve noise and vibration behaviour [30,31].

In the framework of the current study, a hybrid polymer gear is defined as a polymer gear which can house a metallic insert, or any other candidate material with good thermal conductivity and adequate mechanical properties, to improve heat conduction, mechanical resistance and increased gear life. Potential hybrid polymer gear designs have been proposed and studied [1,29].

Fernandes et al. [1] proposed different designs of a metallic insert impregnated in the polymer matrix. These designs promoted better heat conduction, decreasing the teeth' operating temperature and potentially increasing the load-carrying capacity. The previous study was conducted to investigate how the material (steel, aluminium, and copper) and shape of an insert affect the thermal performance of a non-lubricated hybrid polymer gear. The best results were found with an aluminium insert in a simple cuboid shape, balancing thermal performance, mass, and manufacturing feasibility. However, the hybrid gear design has not yet been experimentally validated.

In comparison with the previous works, the main contribution of the present work is the experimental validation and detailed analysis of the interference fit effect on the hybrid polymer gear design concept. Specifically, the study aims to evaluate the feasibility of the hybrid polymer gear by creating a gear rack test specimen and developing a testing system to examine its thermal performance. To understand its thermal and mechanical behaviour, the surface temperature and thermal expansion of the specimens were examined using digital image correlation (DIC). In addition, a finite element model was created and validated through comparison with the experimental results.

## 2. Material and methods

### 2.1. Hybrid rack tooth geometry

In a previous work [1], a hybrid polymer gear concept based on a standard FZG spur gear geometry [32] was proposed. The concept was developed bearing in mind the possibility to use over-moulding technologies. However, such technologies are typically implemented for medium to large production series and involve a high initial investment. The present work used a hybrid rack tooth gear design easily manufacturable using CNC machining to experimentally validate the concept and the numerical models. The design for the hybrid rack tooth can be seen in Fig. 1.

The rack geometry properties can be found in Table 1. The total length of the rack ( $l_{rack}$ ) was defined as three times the value of the reference pitch. The height of the rack body ( $h_{rack}$ ) was made equal to the distance from the pinion root radius ( $r_d$ ) to the shaft radius ( $r_s = 15$  mm) of a pinion with 16 teeth and a profile shift coefficient ( $x_1 = 0.1817$ ) used in [1].

The parametric dimensions of the insert for the hybrid tooth were based on the previous work [1]. It was found out that assuming a non-constant cross section had a positive impact on the hybrid polymer gear concept. However, due to limitations in manufacturing, the current study was carried out using a simple cuboid geometry with rounded corners. The width tolerance was carefully selected to ensure a press fit and adequate contact pressure between the polymer matrix and the insert. Specifically, the polymer rack hole has a width of 2.19 mm and a height of 19.59 mm, while the insert has a width of 2.25 mm and a height of 19.57 mm. Those dimensions assure an interference fit of  $\delta_w = 0.06$  mm in the width direction and a clearance of  $\delta_h = 0.02$  mm in the vertical direction (Table 1).

### 2.2. Rack tooth and insert materials

The material for the polymer gear rack was based on the VDI 2736 guidelines [33] and also followed the suggested materials from previous work [1]. The selected polymeric gear material was a POM copolymer ERTACETAL C (PolyLanema, Portugal), with the physical properties described in Table 2.

The proposed hybrid solutions consists of (1) POM rack tooth with an aluminium insert and (2) POM rack tooth with a highly conductive epoxy resin insert. The thermal and mechanical properties of the aluminium 6061 alloy and the cured resin ER2220 (Electrolube, UK) can be found in Table 2. All candidate solutions can be seen in Fig. 2.

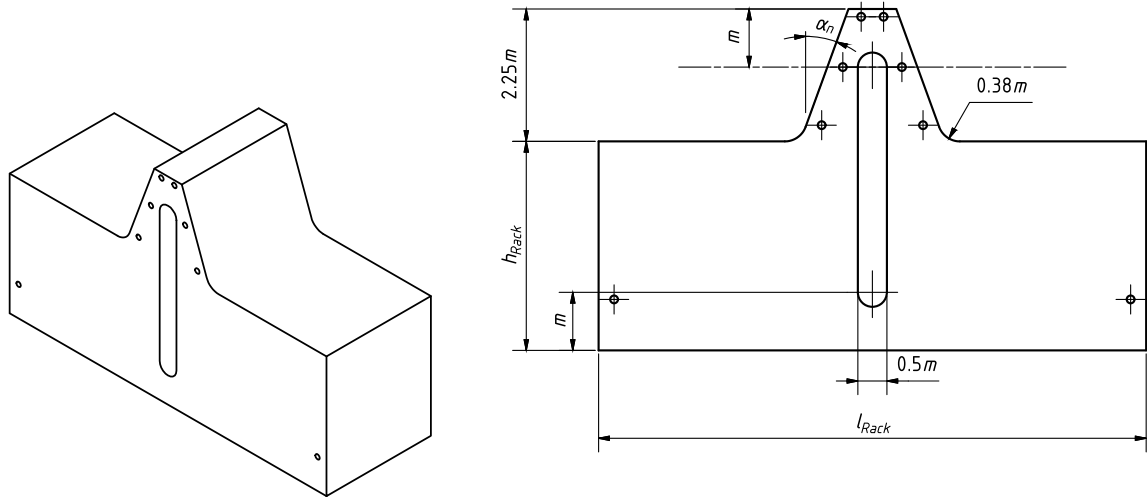


Fig. 1. Hybrid rack tooth model.

**Table 1**  
Gear rack and insert geometry.

Gear rack	
Gear module, $m/\text{mm}$	4.5
Pressure angle, $\alpha_n/^\circ$	20
Root radius coefficient, $\rho$	0.38
Addendum coefficient, $h_{aP}$	1
Deddendum coefficient, $h_{fP}$	1.25
Face width, $b/\text{mm}$	14
Rack length, $l_{\text{Rack}}/\text{mm}$	$3 \cdot \pi \cdot m$
Rack body height, $h_{\text{Rack}}/\text{mm}$	16.19
Insert/hole manufactured geometry	
Insert width/mm	2.25
Hole width/mm	2.19
Width interference fit $\delta_w/\text{mm}$	0.06
Insert height/mm	19.57
Hole height/mm	19.59
Height clearance $\delta_h/\text{mm}$	0.02

**Table 2**  
Mechanical and thermal properties of rack tooth and insert materials.

Property	POM	Aluminium	Epoxy
Thermal conductivity, $\kappa/\text{W m}^{-1} \text{K}^{-1}$	0.31	200	1.54
Thermal expansion, $\alpha/^\circ\text{C}^{-1}$	$1.25 \times 10^{-4}$	$2.31 \times 10^{-5}$	$3.00 \times 10^{-5}$
Density, $\rho/\text{kg m}^{-3}$	1410	2700	2.22
Young's modulus, $E/\text{GPa}$	2.80	69.0	(2.8)
Poisson's ratio	0.35	0.33	(0.43)

### 2.3. Heating system test rig

A test rig was developed specifically to evaluate the thermal behaviour of the hybrid rack teeth. Fig. 3(a) shows the assembly of the heating system with a standard rack tooth, while Fig. 3(b) shows the setup of the type-k thermocouple sensors on the surface of the rack tooth. The rack is fixed to a circular plate, over which dead weights are applied, pressing the tooth against two aluminium supports. These supports, which also house the cartridge heater, have a circular geometry with a radius of 7.5 mm to assure similar contact conditions of the rack against the pinion on the pitch point.

The distance between the two aluminium supports can also be adjusted in order to control the exact point of contact on the flank of the tooth. A hollow cylinder guides the whole set of components attached to the circular plate, i.e., the test specimen and the weights.

The system simultaneously controls the heater temperature and loads the flank of the tooth. Each aluminium support has a circular hole to place a cartridge heater, which will heat up the aluminium, and in turn heat up the test specimen. The cartridge heater and the power source form a closed loop. A resistance thermometer is in contact with the cartridge heater and measures its

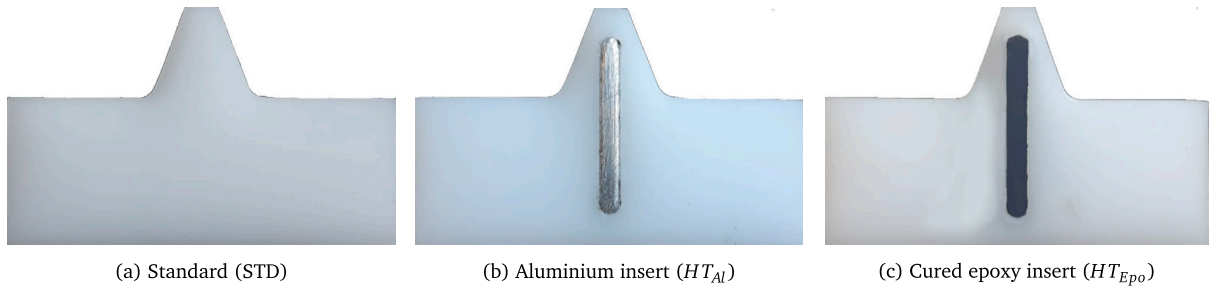
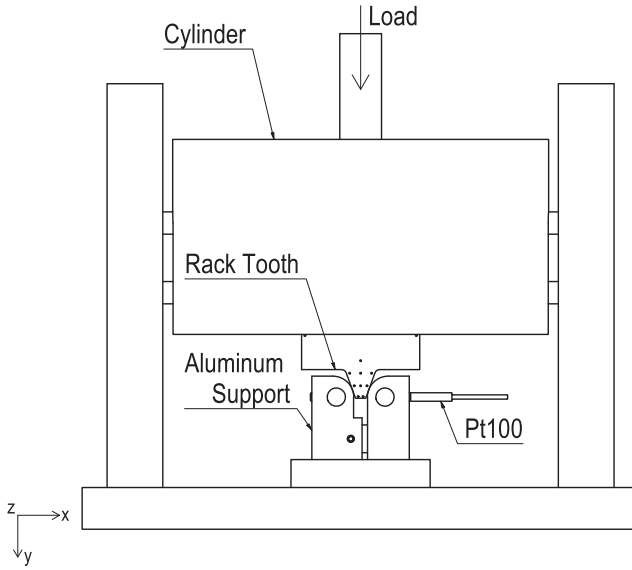
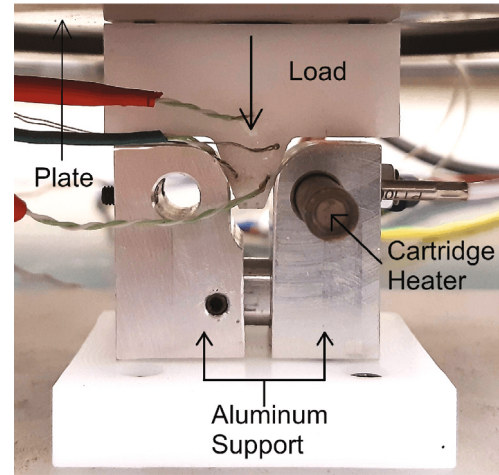


Fig. 2. Gear rack tooth configurations studied.



(a) Front view assembly drawing of the test rig



(b) Aluminium support, heater, rack and thermocouples

Fig. 3. Setup of the standard rack tooth heating system.

temperature. The temperature data returns to the power source, which in turn calibrates the output power to the cartridge heater. This system automatically achieves and maintains the desired output temperature by comparing it with the measured temperature. Due to certain constraints in the experimental setup, it was not feasible to record the data measured by the resistance thermometer. However, to circumvent this limitation, an additional type-k thermocouple was employed to record the temperature of the heater. While this approach allowed us to obtain valuable data, it should be noted that there exists a slight discrepancy between the values obtained via the type-k thermocouple and those recorded by the resistance thermometer.

#### 2.4. Thermocouple sensors

Four thermocouple sensors were attached to the surface of the test specimen in order to measure its temperature during the tests. For this reason, small bore holes were machined on the surface of each tooth to guarantee accurate positioning of the thermocouple sensors. The placement of the thermocouple sensors for the thermal and DIC tests can be seen in Fig. 4. Since the DIC test also includes a thermal analysis, different locations for the thermocouples were selected to gather additional data. The points  $p_R$  and  $p_L$  are respectively the right and left pitch points. The point  $f$  is located close to the tooth root region. The  $b_I$  thermocouple sensor is placed in the main body of the rack while  $b_C$  is close to the lateral and bottom surfaces. The coordinates of the thermocouples are given in Table 3. The surface temperature of the test specimens was recorded using a thermocouple HH306 Datalogger.

#### 2.5. Digital image correlation

DIC is a surface displacement measuring technique that can capture the shape, motion and deformation of solid objects [34]. In most cases, a speckle pattern is applied on the surface of the object being deformed in order to facilitate the tracking process [35].

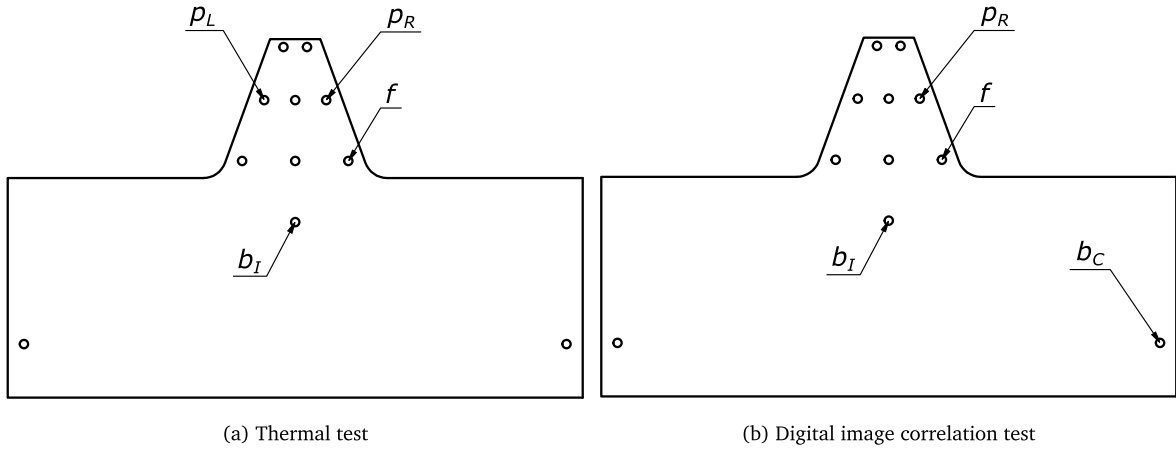


Fig. 4. Thermocouple sensor placement.

Table 3

Location of each thermocouple in relation to the vertical axis of symmetry and tooth dedendum.

Thermocouple	x/mm	y/mm
$p_L$	-2.29	5.75
$p_R$	2.29	5.75
$f$	3.92	1.25
$b_I$	0	-3.25
$b_C$	20.01	-12.25

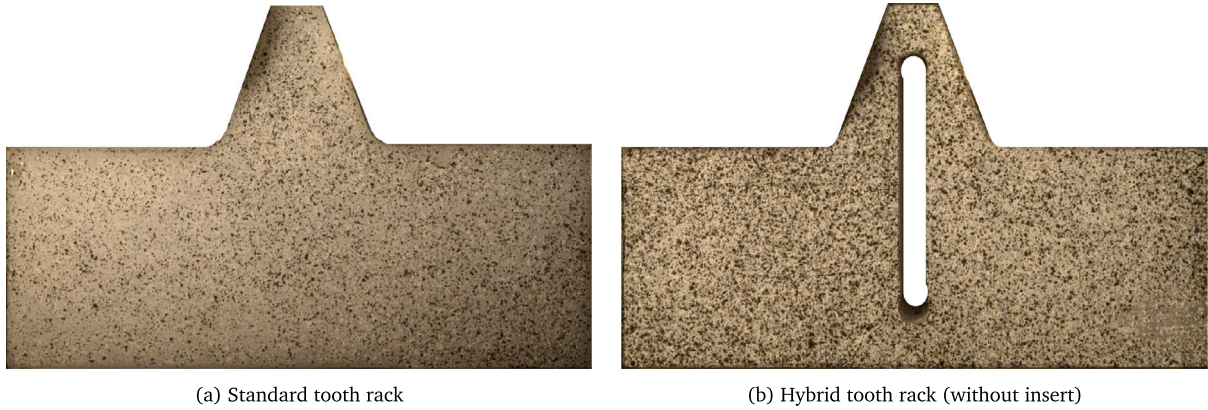


Fig. 5. DIC speckle pattern used.

The pattern moves and deforms with the sample, but should not exert a significant mechanical stress on the sample [34]. DIC has already been applied to measure in-mesh tooth deflection of polymer gears [36].

For the DIC experiment, a single fixed camera was used and the photographs obtained allowed to estimate the displacements and deformations in a selected plane [35]. A speckle pattern was applied on the surface of each test specimen. The methodology of DIC is based on tracking the unique pattern of the speckle in a sequence of images. Consequently, the quality of the speckle pattern affects the accuracy and precision of the displacement results. The speckle pattern for the standard tooth and hybrid tooth can be seen in Fig. 5.

### 3. Test campaign

The thermal and DIC tests were performed for the standard rack tooth, the hybrid rack tooth with an aluminium insert and the hybrid rack tooth with an epoxy insert.

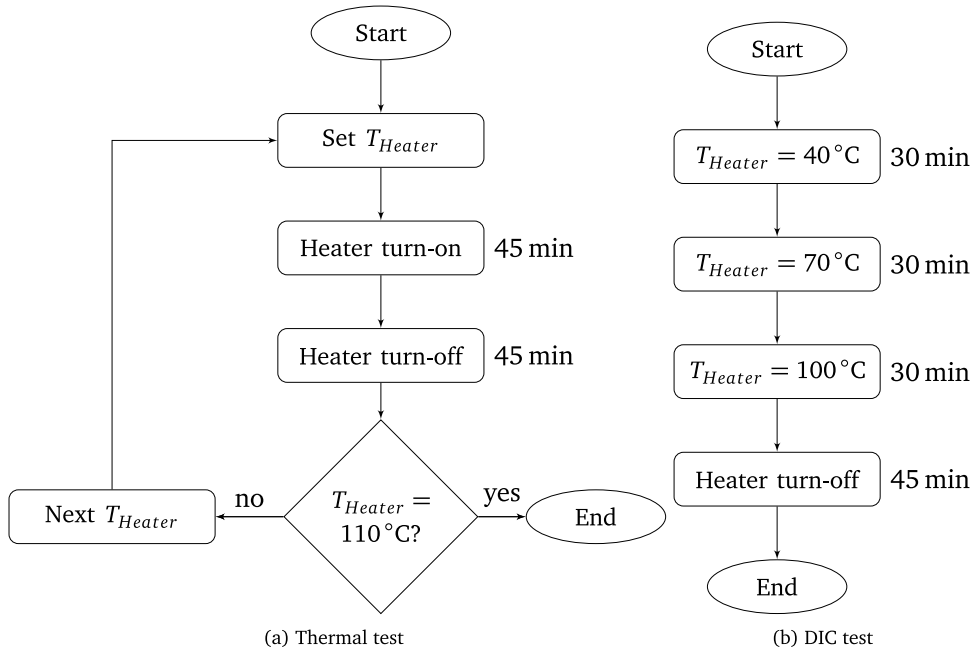


Fig. 6. Test procedure.

### 3.1. Thermal tests

Before mounting the test specimens to the test rig, the thermocouple sensors were attached to its surface. The point of contact between the aluminium supports and the flank of the rack tooth was adjusted to match the pitch point on the tooth's surface, before starting the thermal tests. Next, a total weight of 4.6 kgf was used to fix the test specimen in place. The maximum contact pressure between the specimens and the aluminium support, as a result of the applied weight, is 29.14 MPa. Finally, a single cartridge heater was placed in the aluminium support on the right ( $p_R$ ), as seen in Fig. 3(b).

Once the setup was finished the test was started by turning on the heat source to the desired temperature ( $T_{Heater}$ ). The heating process takes a total of 45 min. Afterwards, the power source was turned off and the system was left to cool at ambient temperature for 45 min. For each test specimen, the test was performed for  $T_{Heater}$  of 40 °C to 110 °C in 10 °C increments. The heating procedure can be seen in Fig. 6(a).

During this procedure the surface temperature was measured with four thermocouple sensors and saved on to a Datalogger.

### 3.2. DIC tests

For the DIC test, the setup of the test rig and test specimen is similar as described before. The speckle pattern was applied to the surface of the test specimen and the four thermocouple sensors were attached to the opposite surface. As before, the test specimen was mounted on the test rig, with the point of contact coinciding with the pitch point of the rack tooth. The same 4.6 kgf was placed to fix the test specimen in place, and a single cartridge heater was placed in the aluminium support on the right ( $p_R$ ).

The test was performed for each test specimen. For the first stage of the test, the temperature of the cartridge heater was set to  $T_{Heater} = 40^{\circ}\text{C}$ . For the second stage, the temperature was increased to  $T_{Heater} = 70^{\circ}\text{C}$ . Finally, in the third phase the temperature was increased to  $T_{Heater} = 100^{\circ}\text{C}$ . Each heating stage had a duration of 30 min. Afterwards, the power source was turned off and the system was left to cool at ambient temperature for 45 min. The DIC test procedure can be seen in Fig. 6(b).

During this process the surface temperature was measured with four thermocouple sensors and saved on to a Datalogger. A single Nikon D3200 (Nikon, Japan) was used to take photographs of the tooth's lateral surface ( $xy$  - plane) every 15 min, capturing the thermal expansion of the test specimen. The images were post-processed with GOM Correlate (Zeiss, Germany) software ensuring that the rigid body motion of the specimens during the tests is removed.

## 4. Thermo-mechanical finite element model

### 4.1. Thermal model

A steady-state model was used to predict the bulk temperature, similarly to the previous works [1,4]. The differential equation that governs the bulk temperature ( $T$ ) distribution within the solid is given by Eq. (1) which reflects the heat flow by conduction [4].



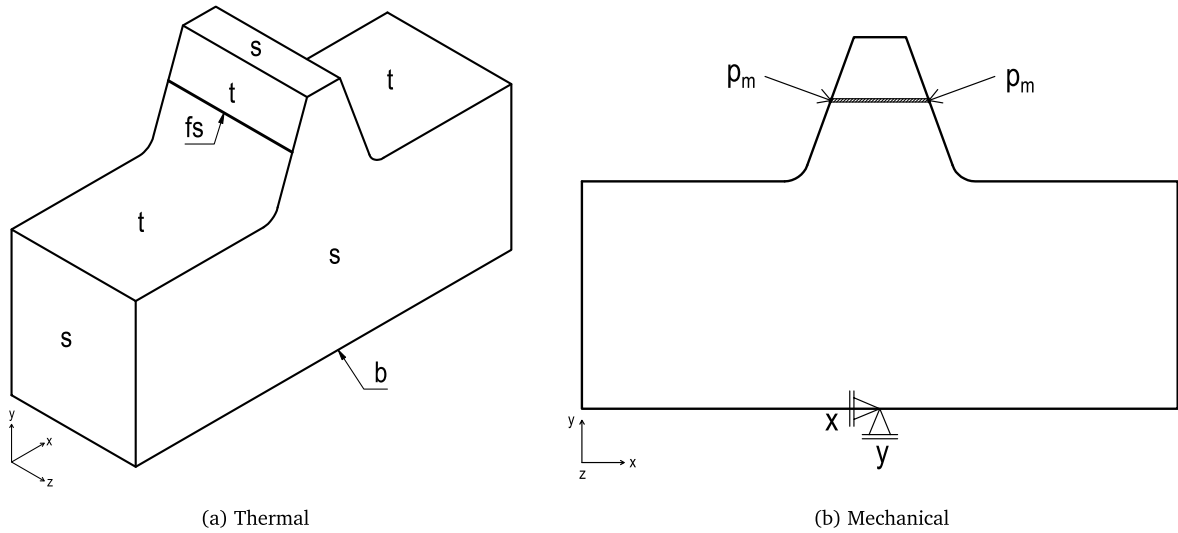


Fig. 7. Surfaces of the rack for which the boundary conditions were set.

$$\kappa \cdot \left( \frac{\partial^2 T}{\partial x^2} + \frac{\partial^2 T}{\partial y^2} + \frac{\partial^2 T}{\partial z^2} \right) = 0 \quad (1)$$

Fig. 7(a) shows the surfaces of the rack for which different boundary conditions were set.

The boundary condition of the gear sides  $s$  in Fig. 7(a), is dependent on the ambient temperature surrounding the tooth ( $T_{air}$ ) and the convective heat transfer coefficient of the gear sides ( $h_s$ ). This boundary condition is given by Eq. (2).

$$-\kappa \cdot \frac{\partial T}{\partial n} \Big|_s = h_s \cdot (T - T_{air}) \quad (2)$$

The boundary condition of the tooth flank in contact with the aluminium support, shown in Fig. 7(a) as the region  $fs$ , is given by Eq. (3). The contact region between the heater's circular profile and the tooth flank can be approximated by a rectangular area whose width is equal to twice the Hertzian contact semi-width ( $a_H = 0.138$  mm) [37]. The Hertz theory is a classical theory widely used to model the contact between two elastic bodies. However, it has certain limitations, particularly when dealing with materials that exhibit non-linear stress-strain behaviour or large displacements. When these conditions are present, the Hertz theory should be used with care, and its predictions should be interpreted with caution.

The temperature of the tooth's surface ( $T_{fs}$ ) in contact with the aluminium support was considered equal to the temperature of the cartridge heater ( $T_{Heater}$ ). The assumption made in this scenario is simplified, as it considers a constant temperature for the heater and disregards thermal contact conductance between the heater and the tooth flank.

$$T_{fs} = T_{Heater} \quad (3)$$

The boundary condition of the top surface of the tooth, referred as  $t$  in Fig. 7(a), is given by Eq. (4). It is dependent on the temperature of the heat source, which is emitting radiation, and the emissivity coefficient of the gear material ( $\epsilon = 0.95$ ).

$$-\kappa \cdot \frac{\partial T}{\partial n} \Big|_t = \epsilon \cdot \sigma \cdot (T_{Heater}^4 - T_{air}^4) + h_t \cdot (T - T_{air}) \quad (4)$$

The bottom surface of the tooth, boundary  $b$  in Fig. 7(a), is in contact with the plate that supports the tooth and weights of the heating system. The heat conduction through this region was neglected and this surface was considered adiabatic ( $\partial T / \partial t = 0$ ) which the experimental results show to be adequate.

The heat transfer coefficient ( $h_s$ ) on boundary  $s$  was determined by assuming that the side surface of the rack is equivalent to a vertical plate. The natural convection heat transfer coefficient ( $h_s$ ) over the surface of the rack is defined here by Eq. (5). Also,  $h_t$  was made equal to  $h_s$ .

$$h_s = \frac{\kappa \cdot Nu}{L_c} \quad (5)$$

The average Nusselt number ( $Nu$ ) for free convection over a vertical wall was calculated by the classical empirical correlation [38]. As the surface temperature changes with height, the heat transfer coefficient was determined by the average temperature observed, resulting in  $h_s = 4 \text{ W m}^{-2} \text{ K}^{-1}$ .

#### 4.2. Mechanical model

Using the Hertz contact theory it is possible to determine the contact pressure generated by the rack tooth flank surface and the circular profile of the aluminium support [37]. As already stated, the maximum contact pressure between the specimens and the aluminium support was 29.14 MPa which corresponds to a mean pressure of 22.89 MPa.

The mechanical model's boundary conditions are closely tied to the design of the test rig. The tooth is fixed to a plate within a cylinder that restricts horizontal movement in the  $x$ -direction. Weights on the opposite side of the plate limit vertical movement in the  $y$ -direction. As a result, the bottom surface of the tooth has a fixed boundary condition in both the  $x$  and  $y$  axis. To prevent rigid motion, the  $z$ -direction is also restricted. Mean contact pressure is applied to the pitch point contact area  $f_s$  on each flank of the tooth.

The three boundary conditions ( $x$ ,  $y$  and  $z$ ) and the mean contact pressure ( $p_m$ ) can be seen in Fig. 7(b).

#### 4.3. Thermo-mechanical model

The model consists of an uncoupled thermal and mechanical FEM analysis. This model combines the effects of the heating process to the tooth flank and the contact pressure during the thermal and DIC tests. The thermo-mechanical model also determines the thermal expansion of the polymer material under these conditions.

#### 4.4. Contact between the polymer and the insert

In order to calculate the thermal contact conductance, it is necessary to determine certain parameters of the contacting surfaces such as the composite root mean square roughness  $\sigma_s$  and the absolute asperity slope  $m_s$ . These values were directly measured for the samples used in this study (see Appendix). According to research by Mikic [39], the elastic deformation in the polymer/metal interface is proportional to the contact pressure and can be calculated based on the ratio between the real contact area  $A_r$  and the apparent contact area  $A_a$  using Eq. (6).

$$\frac{A_r}{A_a} = \frac{p}{H_e} \quad (6)$$

The elastic micro-hardness ( $H_e$ ) of the interface can be calculated using Eq. (7), which takes into account the effective elastic modulus ( $E$ ) of the contacting materials and the absolute asperity slope ( $m_s$ ), similar to the plastic micro-hardness introduced by Yovanovich [40].

$$H_e = \frac{E \cdot m_s}{\sqrt{2}} \quad (7)$$

For the interval between  $10^{-5} \leq p/H_e \leq 0.2$  the dimensionless thermal contact conductance  $C_c$  can be calculated using Eq. (8), considering the equivalent thermal conductivity of the contacting materials ( $k_s$ ).

$$C_c = \frac{h_c \cdot \sigma_s}{k_s \cdot m_s} = 1.54 \cdot \left( \frac{p}{H_e} \right)^{0.94} \quad (8)$$

Fuller et al. [41] suggested using the polymer elastic contact hardness ( $H_{poly}$ ) instead of the elastic contact micro-hardness ( $H_e$ ), as shown in Eq. (9).

$$H_{poly} = \frac{E_{poly} \cdot m_s}{2.3} \quad (9)$$

For polymers, Eq. (10) can be used to calculate the dimensionless thermal contact conductance.

$$C_c = \frac{h_c \cdot \sigma_s}{k_s \cdot m_s} = 1.49 \cdot \left( \frac{p}{H_{poly}} \right)^{0.935} \quad (10)$$

The heat transfer coefficient can be obtained using Eq. (11), which takes into account the thermal contact resistance between the polymer and metallic insert.

$$h_c = 1.49 \cdot \frac{k_s \cdot m_s}{\sigma_s} \cdot \left( \frac{p}{H_{poly}} \right)^{0.935} \quad (11)$$

Experimental investigations have shown that the thermal resistance between contacting surfaces varies with the contact pressure [42]. The influence of the interference fit on the contact pressure was studied using Eq. (11), which considers the thermal contact conductance as a function of the surface roughness, contact pressure, and Young's modulus of the material at the local temperature. The influence of temperature on the Young's modulus of the POM was taken from VDI 2736 [33]. Fig. 8 shows the effect of contact pressure and temperature on thermal contact conductance for  $\sigma_s = 2.32 \mu\text{m}$  (POM/aluminium).

The contact between the metallic insert and the POM rack was set as a surface-to-surface penalty algorithm with linear pressure over-closure. The aluminium insert was set as the master surface and the POM tooth as the slave surface. The thermal contact conductance was calculated based on the local contact pressure and local Young's modulus of the polymer rack material, using the data presented in Fig. 8. The interference fit value was directly imposed on the finite element model mesh.



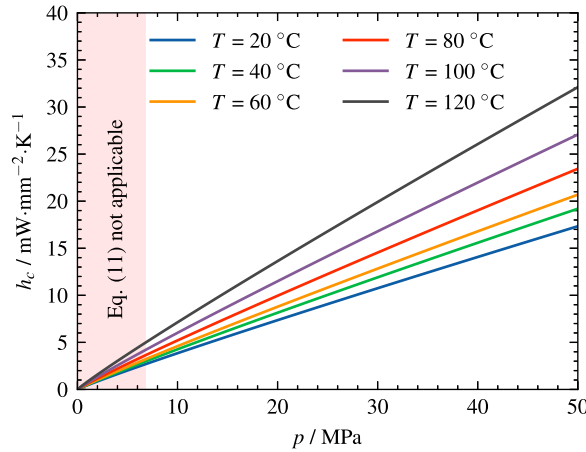


Fig. 8. Effect of contact pressure and temperature on thermal contact conductance for  $\sigma_s = 2.32 \mu\text{m}$  POM/aluminium.

Table 4

Number of mesh elements for each specimen and CPU time.

Specimen	Number of elements	CPU time/s
STD	25344	20
HT <sub>Al</sub>	50112	233
HT <sub>Epo</sub>	50112	39

In the case of  $HT_{Epo}$ , the manufacturing approach employed guarantees adhesion between the insert and the polymer rack without the need for an interference fit. This approach allows for the creation of a unique body in the model mesh, with distinct material properties assigned to each region, thereby eliminating the requirement for a contact formulation. As a result, the solution efficiency is significantly improved.

#### 4.5. Mesh h-Refinement

The finite element analyses were conducted using the CalculiX CrunchiX solver, employing an eight-node brick element type (C3D8) [43]. The structured mesh was generated using Gmsh software [44], and a mesh refinement study was performed for each rack tooth model. The total number of elements was successively increased until the results of the simulation converged. The density of the rack tooth mesh ( $n_M$ ) was generated for each segment as a function of the gear module ( $n_M = \text{int}(N \cdot m)$ ). A h-refinement loop was run ( $N = N + 0.5$ ) until convergence of the results. For each cycle, the results of the average node temperature of the finer mesh were compared with the coarser mesh of the previous cycle, and the relative error was calculated. The mesh convergence occurred for  $N$  equal to 4, with a relative error of 0.30%. Table 4 summarizes the number of elements for each specimen, which varied depending on the presence of an insert in the hybrid geometries.

The models were solved on a laptop equipped with an AMD Ryzen 7 4700U 2.00 GHz CPU and 16 GB of RAM. Table 4 presents the total solution time for each model.

## 5. Results

### 5.1. Temperature measurements

For the duration of the thermal tests, the temperature was recorded every 20 s with an accuracy of  $\pm 1^\circ\text{C}$  and resolution of  $0.1^\circ\text{C}$ . The ambient temperature ( $T_{Amb}$ ) of each test was measured with a mercury thermometer.

The data from the thermal test was exported and plotted over time for each of the four thermocouple measurements. An example of this plot for the STD specimen with  $T_{Heater} = 100^\circ\text{C}$  can be seen in Fig. 9.

The thermocouple sensors  $p_R$  and  $p_L$  represent the temperature measurements closest to the pitch point, as seen in Fig. 4(a), which matches the contact point of the aluminium supports and the flanks of the rack tooth. For this reason, both of these measurements reach the highest temperature values during the test, specially  $p_R$  due to its closest proximity with the heater cartridge.

The thermocouple sensor  $f$  represents the temperature of the tooth root region and the  $b_I$  represents the body temperature of the insert region (see Fig. 4(a)). The  $b_I$  thermocouple sensor is placed the furthest away from the heat source and recorded the lowest temperature during the testing.

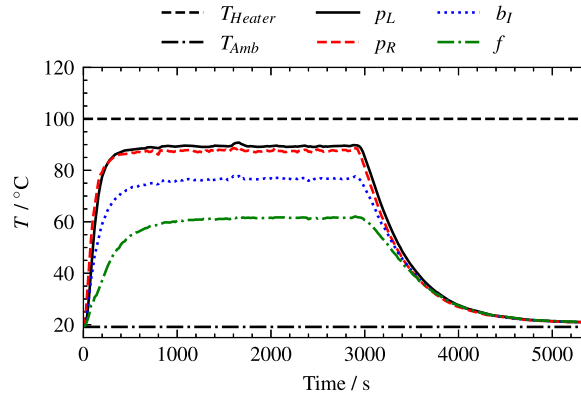


Fig. 9. Temperature measurement of STD for  $T_{Heater} = 100\text{ }^{\circ}\text{C}$ .

The average stabilization temperature ( $\overline{\Delta T} = T_{Avg} - T_{Amb}$ ) was calculated for each of the four temperature measurements. The average temperature ( $T_{Avg}$ ) was calculated for the time interval between 1500 s and 2500 s. Fig. 10 shows the results of the average stabilization temperature  $\overline{\Delta T}$  and standard deviation of the three test specimen.

For the pitch point region ( $p_R$  and  $p_L$ ), both  $STD$  and  $HT_{Epo}$  showed similar temperature results up to  $T_{Heater} = 80\text{ }^{\circ}\text{C}$ , then the  $HT_{Epo}$  showed a temperature difference of up to  $3.4\text{ }^{\circ}\text{C}$  (3.9%) for  $p_R$  and  $2.8\text{ }^{\circ}\text{C}$  (3.3%) for  $p_L$ . The  $HT_{Al}$  showed a lower temperature for this region, in comparison with  $STD$ , with a significant temperature difference of  $14.0\text{ }^{\circ}\text{C}$  (16.0%) for  $p_R$  and  $15.1\text{ }^{\circ}\text{C}$  (18.1%) for  $p_L$ .

For the tooth root region  $f$ , both  $HT_{Al}$  and  $HT_{Epo}$  showed lower temperature in comparison with the  $STD$ , with a temperature difference of  $10.6\text{ }^{\circ}\text{C}$  (14.7%) for  $HT_{Al}$  and  $5.6\text{ }^{\circ}\text{C}$  (7.8%) for  $HT_{Epo}$ .

For the body region ( $b_I$ ), both  $HT_{Al}$  and  $HT_{Epo}$  showed higher temperature in comparison with the  $STD$ , with a temperature difference of  $9.9\text{ }^{\circ}\text{C}$  (20.0%) for  $HT_{Al}$  and  $6.5\text{ }^{\circ}\text{C}$  (13.1%) for  $HT_{Epo}$ .

## 5.2. Displacement measurements

As before, the surface temperature of the test specimens was measured using k-type thermocouple sensors. These sensors were connected to a thermocouple Datalogger, which recorded the temperature data during the tests. In addition to measuring the surface temperature of the specimens, the ambient temperature of each test was also measured using a mercury thermometer. This ambient temperature, denoted as  $T_{Amb}$ , provided a reference point for understanding the temperature variations that occurred during the tests.

The experiments also involved digital image correlation (DIC) tests, in which photographs of the specimens were captured during the testing. These photographs were then post-processed using the GOM Correlate software. The software was used to correct for the rigid body motion of the specimens and to generate a displacement field of the tooth's lateral surface. This displacement field was represented in the  $xy$ -plane and provided information about the deformation of the specimens under load.

Fig. 11 shows an example of the magnitude displacement field for three different types of specimens, referred to as  $STD$ ,  $HT_{Al}$ , and  $HT_{Epo}$ , for a specific test condition with a  $T_{Heater}$  of  $100\text{ }^{\circ}\text{C}$ . The figure illustrates the differences in the thermal expansion between the different specimens and provides an understanding of the behaviour of the hybrid polymer gear rack concept.

Out of the three test specimens, the  $STD$  showed the largest absolute displacement value, which was approximately  $0.19\text{ mm}$ .

The  $HT_{Al}$  specimen, which incorporated an aluminium insert, showed a significant reduction of the thermal expansion of the tooth region. The largest absolute displacement value for this specimen was approximately  $0.15\text{ mm}$ , 11% less in comparison with the standard specimen. Additionally, the displacement field for the  $HT_{Al}$  specimen clearly shows the outline of the aluminium insert, due to its uniform displacement value and much smaller thermal expansion compared to the polymer material.

Similarly, the  $HT_{Epo}$  specimen, which incorporated an epoxy insert, also showed a reduction of the thermal expansion of the tooth region, in particular on the root region. However, the effect was smaller than using an aluminium insert.

## 5.3. FEM model validation

The FEM model was used to predict the temperature field, and the results were presented in Fig. 12. To validate the accuracy of the model, a comparison was made between the model results and experimental data, with the error between the two provided in Table 5. The comparison was facilitated by adding the ambient temperature to the experimental results shown in Fig. 10. For the  $STD$  and  $HT_{Al}$  specimens, the error between the model and experimental results was found to be below 5%, indicating good agreement between the two. However, for the  $b_I$  position on the  $HT_{Epo}$  specimen, the error was larger. Specifically, a larger deviation was observed inside the rack body, where the measured temperature was much smaller than the predicted one. This variation may be due to the inaccurate material properties of the Epoxy resin, which are dependent on the cure protocol, or poor manufacturing

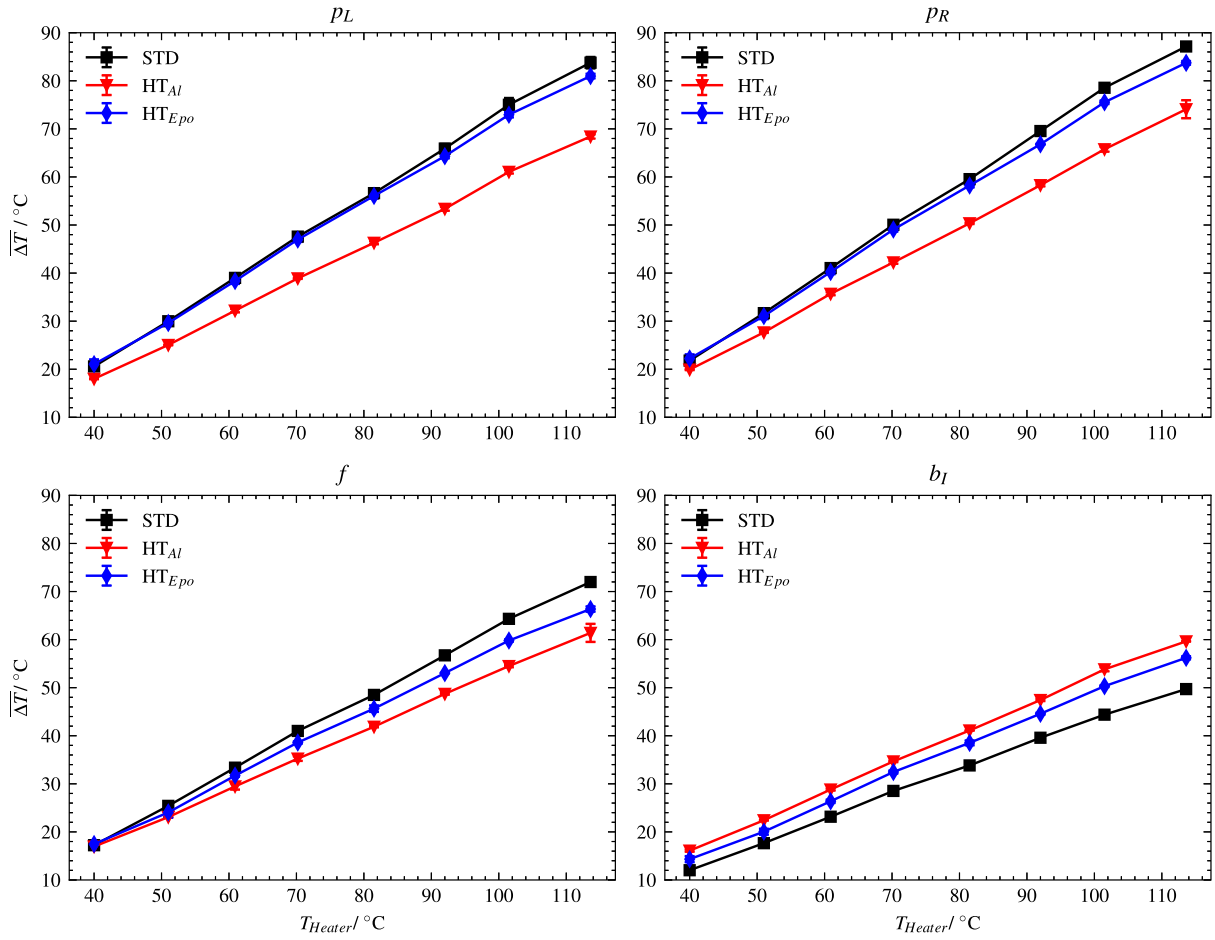


Fig. 10. Average stabilized temperature ( $\overline{\Delta T}$ ) and standard deviation for each test specimen.

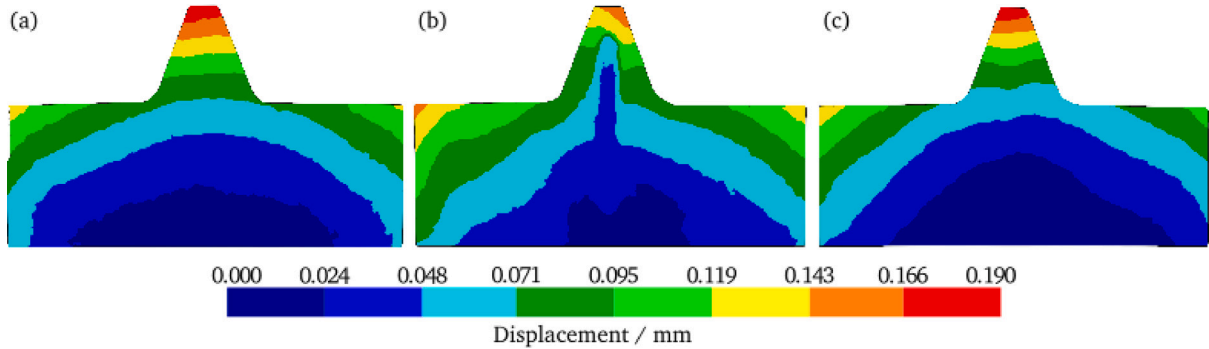


Fig. 11. In-plane displacement field obtained with DIC for  $T_{Heater} = 100$  °C: (a)  $STD$ , (b)  $HT_{Al}$  and (c)  $HT_{Epo}$ .

quality of the proposed solution, affecting the experimental results. Further research is required to fully understand this behaviour. Nevertheless, it can be concluded that for the two models where uncertainties are small, the fitting between the model and the experiments is good.

The magnitude of the displacements of each tooth is shown in Fig. 13 through finite element analysis. A comparison of these results to digital image correlation is presented in Fig. 14 for the  $y$  direction along the vertical axis of symmetry of the rack. The model correlates well for the standard and  $HT_{Al}$  specimens. However,  $HT_{Epo}$  solution presents a weaker correlation between FEM and DIC results. Achieving a perfect match between the FEM model and experimental results requires an entirely precise temperature field, which has not been verified, in addition to accurate thermal material properties. It is important to note that the DIC technique,

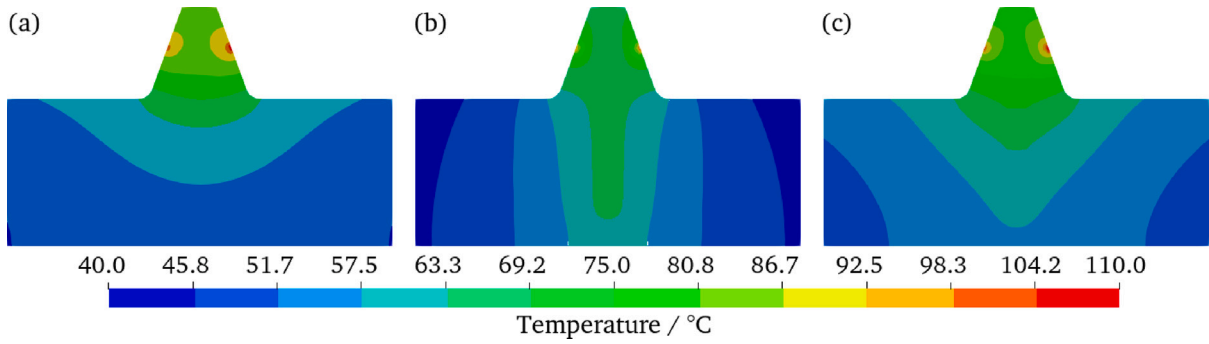


Fig. 12. Temperature field for the side surface for  $T_{Heater} = 100$  °C: (a)  $STD$ , (b)  $HT_{Al}$  and (c)  $HT_{Epo}$ .

Table 5

Error between FEA results and experiments for  $T_{Heater} = 100$  °C.

Specimen	$p_R$			$f$			$b_I$		
	Exp.	FEM	Error	Exp.	FEM	Error	Exp.	FEM	Error
$STD$	93.6	90.2	-3.6%	73.1	73.6	0.7%	66.8	63.5	-4.9%
$HT_{Al}$	77.0	74.2	-3.6%	65.8	64.4	-2.1%	67.5	64.8	-4.0%
$HT_{Epo}$	90.1	86.1	-4.4%	66.3	71.4	7.7%	56.2	63.0	12.1%

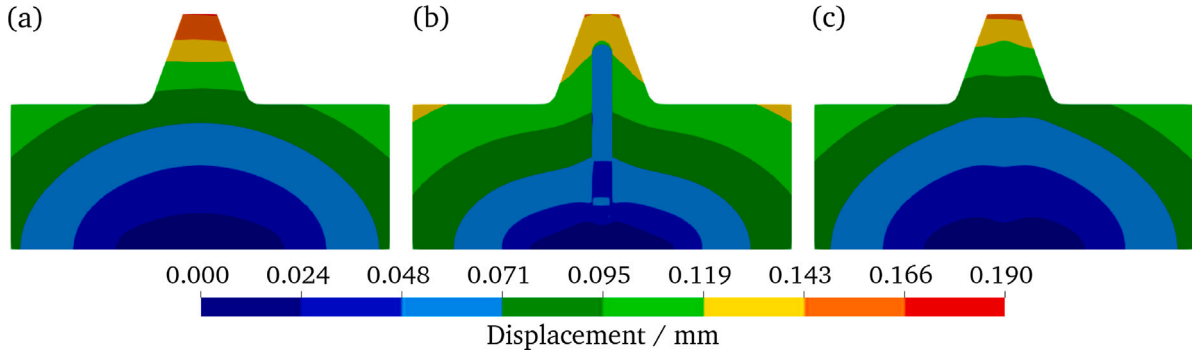


Fig. 13. In-plane displacement field obtained with FEM for  $T_{Heater} = 100$  °C: (a)  $STD$ , (b)  $HT_{Al}$  and (c)  $HT_{Epo}$ .

used to measure experimental displacements, also has associated errors that depend on the quality of the images captured during testing.

## 6. Discussion

### 6.1. Results analysis

In order to study the influence of an insert in a polymer rack tooth, the average stabilized temperature was compared in Fig. 10, and the displacement magnitude was compared in Fig. 11.

Fig. 10 revealed that both hybrid tooth showed a lower temperature in the contact region ( $p_L$  and  $p_R$ ) and tooth root ( $f$ ), and a higher temperature for the body region ( $b_I$ ) putting in evidence the high heat evacuation from the tooth into the rack body. Also, the greater the thermal conductivity of the insert, the more heat evacuation occurs in the tooth region. These results support the conclusions of the previous study [1], which stated that an insert would reduce the maximum bulk temperature and increase the minimum bulk temperature of a polymer gear.

According to the VDI 2736 [18], the limiting strength for the root stress of a POM gear is given by:

$$\sigma_{FlimN} = 26 - 0.0025 \cdot T_f^2 + 400 \cdot N_L^{-0.2}, \quad N_L \in [10^5; 10^8] \quad (12)$$

The increase in limiting strength for  $N_L = 10^6$  is given in Fig. 15(a) while the increase in the expected life ( $N_L$ ) by root failure based on Eq. (12) is estimated in Fig. 15(b) assuming the gear rack is subjected to the same root stress.

The improvement in the maximum strength when  $N_L = 10^6$  is illustrated in Fig. 15(a), estimated using Eq. (12). The expected increase in the life of the gear rack (based on root failure) when subjected to the same root stress is shown in Fig. 15(b).

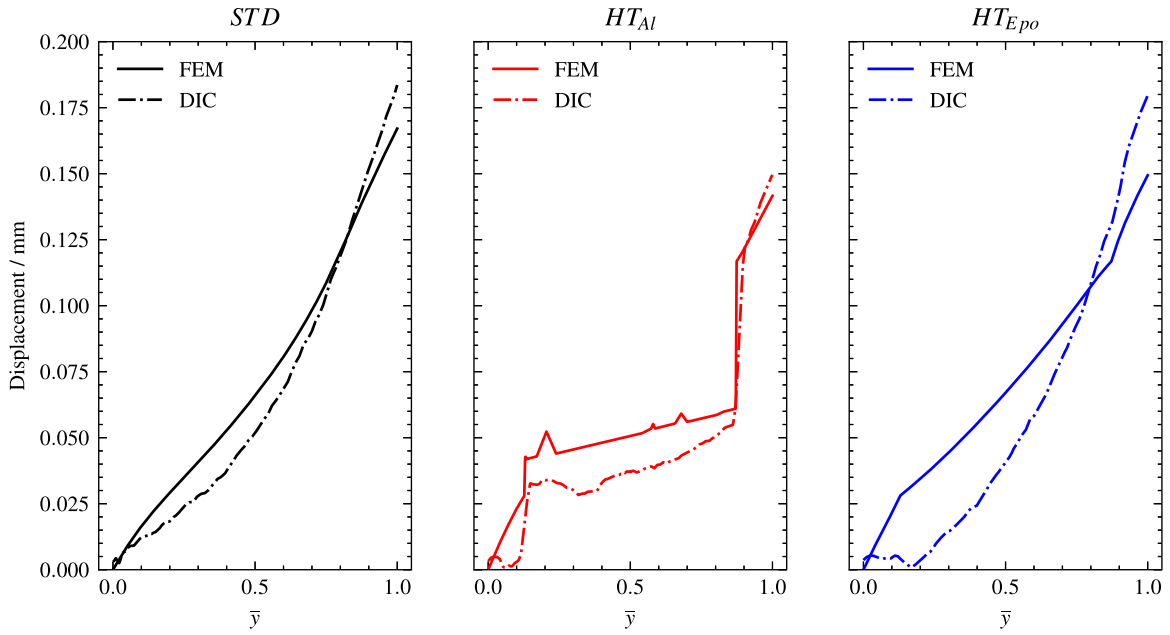


Fig. 14. Comparison between FEM and DIC results for  $T_{Heater} = 100\text{ }^{\circ}\text{C}$ .

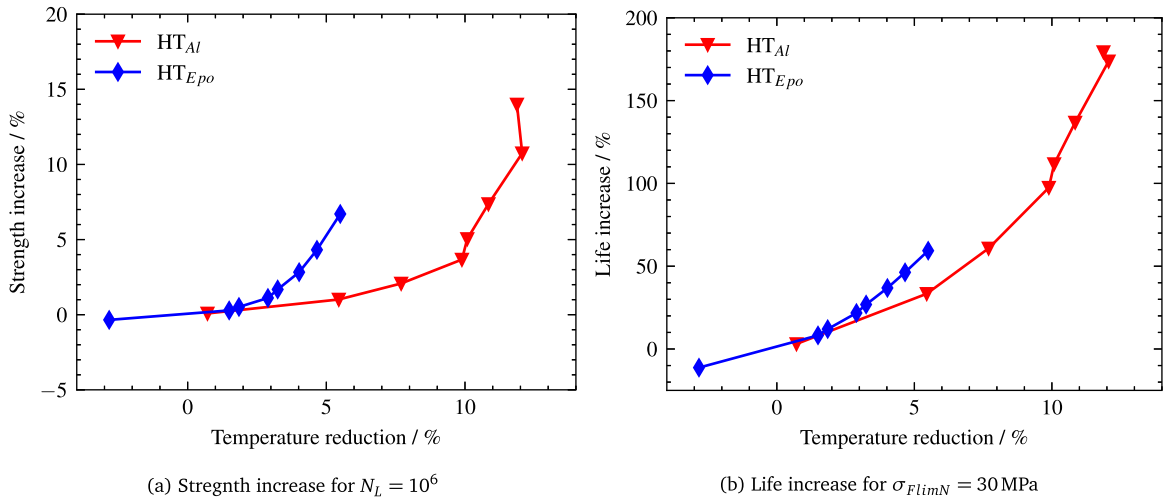


Fig. 15. Expected strength or life increase (root stress) due to temperature decrease.

According to Hasl's research [45], the bending strength of polymer gears is significantly impacted by the substantial increase in contact ratio under load. Therefore, the anticipated increase in stiffness resulting from the incorporation of a metallic insert may offset some of the advantages gained by decreasing the temperature. Consequently, it is essential to conduct additional detailed studies to verify this phenomenon and ascertain whether the reduction in temperature is counteracted by the alteration in gear stiffness [46].

Fig. 11 illustrates that the thermal expansion of the *STD* and *HT<sub>Epo</sub>* specimens followed a similar pattern. The *HT<sub>Al</sub>* specimen, however, exhibited a smaller thermal expansion in the tooth region and a smaller displacement gradient. This is due to the fact that the aluminium insert expands less than the POM matrix, which may lead to an increase in stress concentration in the insert region. On the other hand, the epoxy insert did not exhibit the same trend as the aluminium insert, instead, its thermal expansion was similar to the POM matrix. Thus, an ideal insert should be a highly conductive material with similar mechanical properties as the polymer matrix.

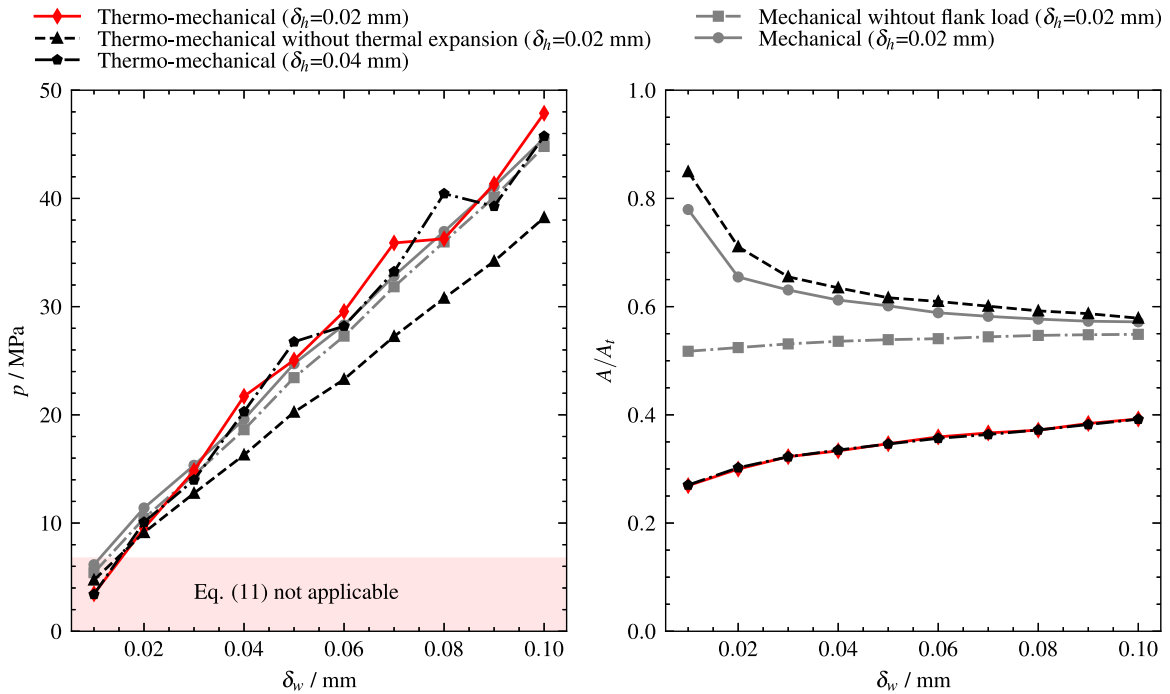


Fig. 16. Influence of the interference fit on the mean contact pressure and relative contact area between the aluminium insert and polymer tooth obtained using FEM model.

## 6.2. Influence of interference fit on performance of $HT_{Al}$

The experiments and FEM model of the  $HT_{Al}$  specimen showed good fitting. As a result, the average contact pressure between the insert and the polymer was determined for various interference fit values using different modelling strategies. These strategies included a mechanical FEM model without load applied on the tooth flanks, a mechanical FEM model with load applied on the flanks, and the thermo-mechanical FEM model proposed in this study, which can consider thermal expansion as well as different height clearances. The results of these analyses are presented in Fig. 16. Based on the findings, it can be inferred that the manufacturing dimensions utilized in this study (Table 1,  $\delta_w = 0.06$  mm) can produce a contact pressure resulting from the width interference fit, which falls within the range of applicability of Eq. (11).

The analysis of the results presented in Fig. 16 shows that the average contact pressure between the insert and the polymer rack is similar across all modelling strategies. For an increasing prescribed interference fit, a higher difference between the maximum and minimum local contact pressure calculated was observed, mainly for the thermo-mechanical solutions.

To better present the differences among modelling strategies, the contact area between the insert and the polymer tooth was taken from the FEM model. To quantify this, the ratio between the FEM contact area ( $A$ ) and the total contactable area of the insert ( $A_t$ ) was calculated for each model configuration. Comparing the results obtained from the FEM mechanical models reveals that for a small interference fit, the application of load on the tooth flanks increases the contact area. A similar behaviour is observed for the FEM thermo-mechanical model without thermal expansion. However, the consideration of thermal expansion substantially decreases the contact area, suggesting that the proposed concept can be further optimized to improve the thermal contact conductance. It is worth noting that the specimens studied in this research had lateral faces of the gear rack that were free to move, which may explain why the contact area decreases when considering the thermal expansion of the polymer.

The height direction was designed with some clearance to avoid stress concentration in regions with a small radius. To verify that the clearance has a negligible effect on the concept, two longitudinal clearances were studied: the one used in the current study (Table 1,  $\delta_h = 0.02$  mm) and one two times larger. The results (Fig. 16) show that the influence is unnoticeable.

Overall, these findings demonstrate the importance of the proposed modelling strategy and parameters when studying the thermal behaviour of polymer racks with inserts. The proposed concept shows promise for improving heat dissipation in gear racks and similar systems, and further optimization could lead to better results.

## 7. Conclusions

In this article, a hybrid polymer gear concept was studied and validated using a rack tooth geometry. The following conclusions were achieved:



- The hybrid polymer gear showed an increase of heat evacuation from the tooth to the polymer body. It was effective in reducing the maximum bulk temperature and increasing the minimum bulk temperature;
- The  $HT_{Al}$  reduced the maximum body temperature by 15.0% and increased the minimum temperature by 20.0%. The  $HT_{Epo}$  reduced the maximum body temperature by 3.4% and increased the minimum temperature by 13.1%;
- The thermal conductivity coefficient of the insert material significantly impacts the effectiveness of the heat evacuation;
- The hybrid polymer gear showed a reduction of the thermal expansion of the tooth region. The  $HT_{Al}$  showed an incompatible thermal expansion for the insert region, which could lead to an increase of stress or gear failure;
- The finite element analysis revealed that the proposed concept can be optimized to enhance the contact area between the insert and the tooth during operation. This optimization will help counterbalance the effects of polymer thermal expansion, ensuring improved performance of the system;
- The ideal insert should be a highly conductive material with similar mechanical properties as the polymer matrix.

### CRedit authorship contribution statement

**James D.S. Hooton:** Test rig design, Experiments, Software, Formal analysis, Investigation, Writing – original draft. **David E.P. Gonçalves:** Methodology, Supervision, Validation, Investigation, Writing – review & editing. **Carlos M.C.G. Fernandes:** Conceptualization, Methodology, Software, Surface Analysis, Validation, Investigation, Writing – review & editing.

### Declaration of competing interest

The authors declare that they have no conflicts of interest.

### Data availability

Data will be made available on request.

### Acknowledgements

The authors are grateful for:

- Professor Jorge H.O. Seabra for the valuable suggestions for the present study;
- the funding through LAETA, Portugal in the framework of project UID/50022/2020.

### Appendix. Surface roughness characterization

The surface roughness of the specimens was measured using a Hommelwerke T8000 controller with a linear unit LV-50 (Hommelwerke GmbH, Germany). The stylus probe has a vertical measurement range of  $\pm 300\mu\text{m}$ , a tip radius of  $5\mu\text{m}$  and a cone angle of  $90^\circ$ . An evaluation area of  $7.5\text{ mm} \times 3\text{ mm}$  was performed for the current study. The topographies are presented in Fig. A.17 after form removal and the application of a cut-off filter of  $0.8\text{ mm}$ . The areal surface roughness parameters of the specimens were determined as per ISO 25178-2. The results are given in Table A.6.

The composite roughness of the contacting surfaces was obtained by the following equation:

$$\sigma_s = \sqrt{Rq_{hole}^2 + Rq_{insert}^2} \quad (\text{A.1})$$

The effective mean absolute asperity slope of the interface was estimated by:

$$m_s = 0.125 \cdot \sigma_s^{0.402} \quad (\text{A.2})$$

**Table A.6**  
Areal surface parameters of  $HT_{Al}$  parts.

Parameter	Hole	Insert	Description
Sa/ $\mu\text{m}$	1.60	0.86	arithmetical mean height
Sq/ $\mu\text{m}$	2.02	1.15	root mean square height
Sp/ $\mu\text{m}$	11.40	6.42	maximum peak height
Sv/ $\mu\text{m}$	9.01	10.20	maximum pit height
Ssk	−0.50	−1.05	skewness
Sku	3.28	5.57	kurtosis
Sz	20.40	16.6	maximum height
$\sigma_s/\mu\text{m}$	2.32		composite roughness
$m_s$	0.175		absolute asperity slope

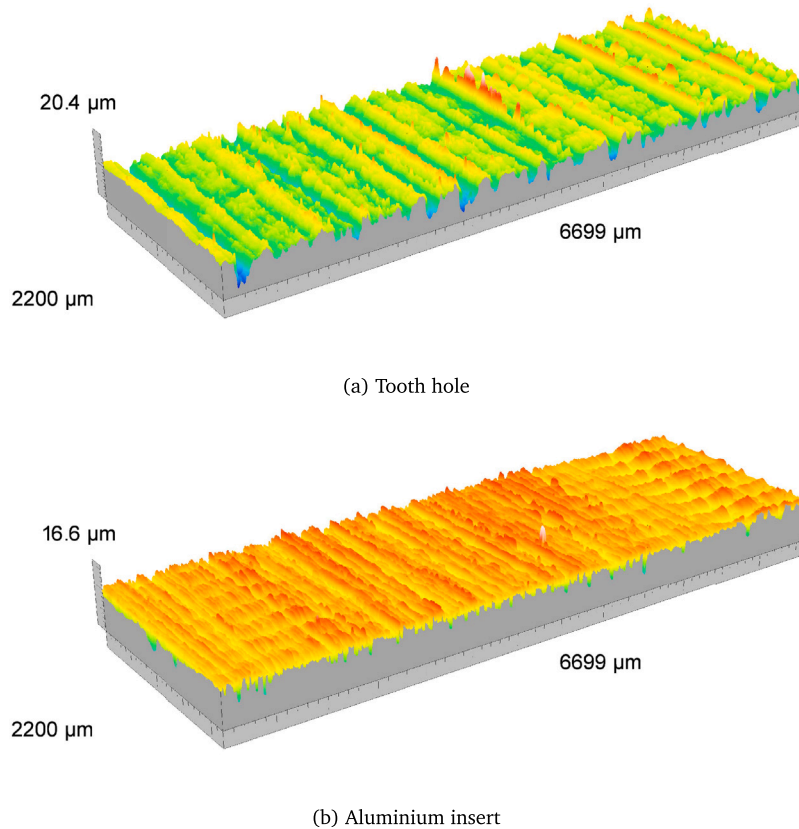


Fig. A.17. Surface topographies of the tooth hole and insert of  $HT_{Al}$ .

## References

- [1] C.M. Fernandes, D.M. Rocha, R.C. Martins, L. Magalhães, J.H. Seabra, Hybrid polymer gear concepts to improve thermal behavior, *J. Tribol.* 141 (3) (2019) 032201, <http://dx.doi.org/10.1115/1.4041461>.
- [2] K. Mao, W. Li, C.J. Hooke, D. Walton, Friction and wear behaviour of acetal and nylon gears, *Wear* 267 (1–4) (2009) 639–645, <http://dx.doi.org/10.1016/j.wear.2008.10.005>.
- [3] M. Jain, S. Patil, A review on materials and performance characteristics of polymer gears, *Proc. Inst. Mech. Eng. C* (2023) 09544062221142155, <http://dx.doi.org/10.1177/09544062221142155>.
- [4] C.M. Fernandes, D.M. Rocha, R.C. Martins, L. Magalhães, J.H. Seabra, Finite element method model to predict bulk and flash temperatures on polymer gears, *Tribol. Int.* 120 (2018) 255–268, <http://dx.doi.org/10.1016/J.TRIBOINT.2017.12.027>.
- [5] M. Hribersek, M. Erjavec, G. Hlebanja, S. Kulovec, Durability testing and characterization of POM gears, *Eng. Fail. Anal.* 124 (2020) (2021) 105377, <http://dx.doi.org/10.1016/j.engfailanal.2021.105377>.
- [6] D. Zorko, S. Kulovec, J. Duhovnik, J. Tavčar, Durability and design parameters of a steel/peek gear pair, *Mech. Mach. Theory* 140 (2019) 825–846, <http://dx.doi.org/10.1016/j.mechmachtheory.2019.07.001>.
- [7] K. Mao, W. Li, C. Hooke, D. Walton, Polymer gear surface thermal wear and its performance prediction, *Tribol. Int.* 43 (1) (2010) 433–439, <http://dx.doi.org/10.1016/j.triboint.2009.07.006>.
- [8] M. Kalin, A. Kupec, The dominant effect of temperature on the fatigue behaviour of polymer gears, *Wear* 376–377 (2017) 1339–1346, <http://dx.doi.org/10.1016/j.wear.2017.02.003>, 21st International Conference on Wear of Materials.
- [9] S. Matković, A. Pogačnik, M. Kalin, Wear-coefficient analyses for polymer-gear life-time predictions: A critical appraisal of methodologies, *Wear* 480–481 (2021) 203944, <http://dx.doi.org/10.1016/j.wear.2021.203944>.
- [10] U. Urbas, D. Zorko, B. Černe, J. Tavčar, N. Vukašinović, A method for enhanced polymer spur gear inspection based on 3D optical metrology, *Measurement* 169 (2021) 108584, <http://dx.doi.org/10.1016/j.measurement.2020.108584>.
- [11] U. Urbas, D. Zorko, N. Vukašinović, B. Černe, Comprehensive areal geometric quality characterisation of injection moulded thermoplastic gears, *Polymers* 14 (4) (2022) <http://dx.doi.org/10.3390/polym14040705>.
- [12] J. Tavčar, B. Černe, J. Duhovnik, D. Zorko, A multicriteria function for polymer gear design optimization, *J. Comput. Des. Eng.* 8 (2) (2021) 581–599, <http://dx.doi.org/10.1093/jcde/qwaa097>.
- [13] H. Hachmann, E. Strickle, Polyamide als zahnradwerkstoffe, *Konstruktion* 18 (3) (1966) 81–94.
- [14] S. Takanashi, A. Shoji, Über den temperaturanstieg von zähnen von kunststoffzahnradern (2, Bericht): Über die gleichgewichtstemperatur von zähnen von kunststoffzahnradern, *Sci. Rep. Res. Inst. Tohoku Univ. Ser. A Phys. Chem. Metall.* 28 (1979) 103–115.
- [15] S. Takanashi, A. Shoji, On the temperature rise in the teeth of plastic gears, in: *International Power Transmission & Gearing Conference*, San Francisco, 1980.
- [16] S. Takanashi, A. Shoji, On the equilibrium temperature in the teeth of operating plastic gears, *Bull. Yamagata Univ.* 18 (1) (1984) 11–24.

- [17] K. Mao, The Performance of Dry Running Non-Metallic Gears (Ph.D. thesis), School of Manufacturing and Mechanical Engineering, The University of Birmingham, 1993.
- [18] VDI-2736 Blatt 2: Thermoplastic Gear Wheels - Cylindrical Gears - Calculation of the Load-Carrying Capacity, Standard, Verein Deutscher Ingenieure, Dusseldorf, DE, 2013.
- [19] V. Roda-Casanova, C.M. Fernandes, A comparison of analytical methods to predict the bulk temperature in polymer spur gears, *Mech. Mach. Theory* 173 (2022) 104849, <http://dx.doi.org/10.1016/j.mechmachtheory.2022.104849>.
- [20] K. Mao, A numerical method for polymer composite gear flash temperature prediction, *Wear* 262 (2007) 1321–1329, <http://dx.doi.org/10.1016/j.wear.2007.01.008>.
- [21] W. Li, P. Zhai, J. Tian, B. Luo, Thermal analysis of helical gear transmission system considering machining and installation error, *Int. J. Mech. Sci.* 149 (September) (2018) 1–17, <http://dx.doi.org/10.1016/j.ijmecsci.2018.09.036>.
- [22] V. Roda-Casanova, F. Sanchez-Marin, A 2D finite element based approach to predict the temperature field in polymer spur gear transmissions, *Mech. Mach. Theory* 133 (2019) 195–210, <http://dx.doi.org/10.1016/j.mechmachtheory.2018.11.019>.
- [23] B. Černe, J. Duhovnik, J. Tavčar, Semi-analytical flash temperature model for thermoplastic polymer spur gears with consideration of linear thermo-mechanical material characteristics, *J. Comput. Des. Eng.* 6 (4) (2019) 617–628, <http://dx.doi.org/10.1016/j.jcde.2019.03.001>.
- [24] B. Černe, M. Petkovšek, J. Duhovnik, J. Tavčar, Thermo-mechanical modeling of polymer spur gears with experimental validation using high-speed infrared thermography, *Mech. Mach. Theory* 146 (2020) 103734, <http://dx.doi.org/10.1016/j.mechmachtheory.2019.103734>.
- [25] Z. Lu, H. Liu, P. Wei, C. Zhu, D. Xin, Y. Shen, The effect of injection molding lunker defect on the durability performance of polymer gears, *Int. J. Mech. Sci.* 180 (2020) 105665, <http://dx.doi.org/10.1016/j.ijmecsci.2020.105665>.
- [26] V. Roda-Casanova, F. Sanchez-Marin, R. Martinez-Cuenca, Convective heat transfer modelling in dry-running polymer spur gears, *Int. J. Mech. Sci.* (2022) 107927, <http://dx.doi.org/10.1016/j.ijmecsci.2022.107927>.
- [27] H. İmrek, Performance improvement method for nylon 6 spur gears, *Tribol. Int.* 42 (3) (2009) 503–510, <http://dx.doi.org/10.1016/j.triboint.2008.08.011>.
- [28] P.K. Singh, Siddhartha, A.K. Singh, An investigation on the effects of the various techniques over the performance and durability of polymer gears, *Mater. Today: Proc.* 4 (2, Part A) (2017) 1606–1614, <http://dx.doi.org/10.1016/j.matpr.2017.01.184>, 5th International Conference of Materials Processing and Characterization (ICMPC 2016).
- [29] C.H. Kim, Durability improvement method for plastic spur gears, *Tribol. Int.* 39 (11) (2006) 1454–1461, <http://dx.doi.org/10.1016/j.triboint.2006.01.020>.
- [30] A. Rezayat, P.G. Catera, C. Capalbo, F. Cosco, D. Mundo, Numerical and experimental analysis of the transmission error in hybrid metal-composite gears, *Compos. Struct.* 298 (2022) 116012, <http://dx.doi.org/10.1016/j.compstruct.2022.116012>.
- [31] F. Cosco, R. Adduci, L. Muzzi, A. Rezayat, D. Mundo, Multiobjective design optimization of lightweight gears, *Machines* 10 (9) (2022) <http://dx.doi.org/10.3390/machines10090779>.
- [32] C.M. Fernandes, R.C. Martins, J.H. Seabra, Torque loss of type C40 FZG gears lubricated with wind turbine gear oils, *Tribol. Int.* 70 (2014) 83–93, <http://dx.doi.org/10.1016/j.triboint.2013.10.003>.
- [33] VDI-2736 Blatt 1: Thermoplastic gear wheels - Materials, material selection, production methods, production tolerances, form design, Standard, 2013, Verein Deutscher Ingenieure, Dusseldorf, DE.
- [34] S.N. Olufsen, M.E. Andersen, E. Fagerholt,  $\mu$ DIC: An open-source toolkit for digital image correlation, *SoftwareX* 11 (2020) 100391, <http://dx.doi.org/10.1016/j.softx.2019.100391>.
- [35] W.S. LePage, J.A. Shaw, S.H. Daly, Optimum paint sequence for speckle patterns in digital image correlation, *Exp. Tech.* 41 (5) (2017) 557–563, <http://dx.doi.org/10.1007/s40799-017-0192-3>.
- [36] B. Černe, M. Petkovšek, High-speed camera-based optical measurement methods for in-mesh tooth deflection analysis of thermoplastic spur gears, *Mater. Des.* 223 (2022) 111184, <http://dx.doi.org/10.1016/j.matdes.2022.111184>.
- [37] H. Hertz, *Miscellaneous Papers*, Macmillan, 1896.
- [38] Y. Çengel, A. Ghajar, *Heat and Mass Transfer: Fundamentals & Applications*, Asia Higher Education Engineering/Computer Science Mechanical Engineering, McGraw Hill Education, 2015.
- [39] B. Mikic, Thermal contact conductance: Theoretical considerations, *Int. J. Heat Mass Transfer* 17 (2) (1974) 205–214.
- [40] M.M. Yovanovich, Thermal contact correlations. Progress in aeronautics and aerodynamics: Spacecraft radiative transfer and temperature control, *AIAA J.* 20 (1982) 102–150.
- [41] J.J. Fuller, E.E. Marotta, Thermal contact conductance of metal/polymer joints: An analytical and experimental investigation, *J. Thermophys. Heat Transfer* 15 (2) (2001) 228–238.
- [42] T.L. Bergam, A.S. Lavine, F.P. Incropera, D.P. Dewitt, *Fundamentals of Heat and Mass Transfer*, seventh ed., John Wiley & Sons, 2011.
- [43] G. Dhondt, *The Finite Element Method for Three-Dimensional Thermomechanical Applications*, John Wiley & Sons, Ltd, 2004.
- [44] C. Geuzaine, J.F. Remacle, Gmsh: A 3-D finite element mesh generator with built-in pre- and post-processing facilities, *Internat. J. Numer. Methods Engrg.* 79 (11) (2009) 1309–1331, <http://dx.doi.org/10.1002/nme.2579>.
- [45] C. Hasl, H. Liu, P. Oster, T. Tobie, K. Stahl, Forschungsstelle fuer Zahnraeder und Getriebbau (Gear Research Centre), method for calculating the tooth root stress of plastic spur gears meshing with steel gears under consideration of deflection-induced load sharing, *Mech. Mach. Theory* 111 (2017) 152–163, <http://dx.doi.org/10.1016/j.mechmachtheory.2017.01.015>.
- [46] A.E. Chakroun, C. Hammami, A. Hammami, A. De-Juan, F. Chaari, A. Fernandez, F. Viadero, M. Haddar, Gear mesh stiffness of polymer-metal spur gear system using generalized Maxwell model, *Mech. Mach. Theory* 175 (2022) 104934, <http://dx.doi.org/10.1016/j.mechmachtheory.2022.104934>.